



# Asteroseismology of $\iota$ Draconis and Discovery of an Additional Long-period Companion

Michelle L. Hill<sup>1</sup> , Stephen R. Kane<sup>1</sup> , Tiago L. Campante<sup>2,3</sup> , Zhexing Li<sup>1</sup> , Paul A. Dalba<sup>1,25</sup> , Timothy D. Brandt<sup>4</sup> , Timothy R. White<sup>5</sup> , Benjamin J. S. Pope<sup>6,7</sup> , Keivan G. Stassun<sup>8</sup> , Benjamin J. Fulton<sup>9</sup> , Enrico Corsaro<sup>10</sup> , Tanda Li<sup>11,12</sup> , J. M. Joel Ong<sup>13</sup> , Timothy R. Bedding<sup>5,12</sup> , Diego Bossini<sup>2</sup> , Derek L. Buzasi<sup>14</sup> , William J. Chaplin<sup>11,12</sup> , Margarida S. Cunha<sup>2</sup> , Rafael A. García<sup>15</sup> , Sylvain N. Breton<sup>15</sup> , Marc Hon<sup>16,17</sup> , Daniel Huber<sup>16</sup> , Chen Jiang<sup>18,19</sup> , CenK Kayhan<sup>20</sup> , James S. Kuszlewicz<sup>12,18</sup> , Savita Mathur<sup>21,22</sup> , Aldo Serenelli<sup>23,24</sup> , and Dennis Stello<sup>12,17</sup>

<sup>1</sup> Department of Earth and Planetary Sciences, University of California, Riverside, CA 92521, USA; [mhill012@ucr.edu](mailto:mhill012@ucr.edu)

<sup>2</sup> Instituto de Astrofísica e Ciências do Espaço, Universidade do Porto, Rua das Estrelas, 4150-762 Porto, Portugal

<sup>3</sup> Departamento de Física e Astronomia, Faculdade de Ciências da Universidade do Porto, Rua do Campo Alegre, s/n, 4169-007 Porto, Portugal

<sup>4</sup> Department of Physics, University of California, Santa Barbara, Santa Barbara, CA 93106, USA

<sup>5</sup> Sydney Institute for Astronomy (SIfA), School of Physics, University of Sydney, NSW 2006, Australia

<sup>6</sup> School of Mathematics and Physics, The University of Queensland, St Lucia, QLD 4072, Australia

<sup>7</sup> Centre for Astrophysics, University of Southern Queensland, West Street, Toowoomba, QLD 4350, Australia

<sup>8</sup> Vanderbilt University, Department of Physics & Astronomy, 6301 Stevenson Center Lane, Nashville, TN 37235, USA

<sup>9</sup> NASA Exoplanet Science Institute/Caltech-IPAC, MC 314-6, 1200 E California Boulevard, Pasadena, CA 91125, USA

<sup>10</sup> INAF—Osservatorio Astrofisico di Catania, via S. Sofia 78, I-95123 Catania, Italy

<sup>11</sup> School of Physics and Astronomy, University of Birmingham, Edgbaston, Birmingham B15 2TT, UK

<sup>12</sup> Stellar Astrophysics Centre (SAC), Department of Physics and Astronomy, Aarhus University, Ny Munkegade 120, DK-8000 Aarhus C, Denmark

<sup>13</sup> Department of Astronomy, Yale University, 52 Hillhouse Avenue, New Haven, CT 06511, USA

<sup>14</sup> Department of Chemistry and Physics, Florida Gulf Coast University, 10501 FGCU Boulevard S., Fort Myers, FL 33965, USA

<sup>15</sup> AIM, CEA, CNRS, Université Paris-Saclay, Université Paris Diderot, Sorbonne Paris Cité, F-91191 Gif-sur-Yvette, France

<sup>16</sup> Institute for Astronomy, University of Hawai'i, 2680 Woodlawn Drive, Honolulu, HI 96822, USA

<sup>17</sup> School of Physics, The University of New South Wales, Sydney, NSW 2052, Australia

<sup>18</sup> Max-Planck-Institut für Sonnensystemforschung, Justus-von-Liebig-Weg 3, D-37077 Göttingen, Germany

<sup>19</sup> School of Physics and Astronomy, Sun Yat-Sen University, No. 135, Xingang Xi Road, Guangzhou 510275, People's Republic of China

<sup>20</sup> Department of Astronomy and Space Sciences, Erciyes University, 38030, Kayseri, Turkey

<sup>21</sup> Instituto de Astrofísica de Canarias (IAC), E-38205 La Laguna, Tenerife, Spain

<sup>22</sup> Universidad de La Laguna (ULL), Departamento de Astrofísica, E-38206 La Laguna, Tenerife, Spain

<sup>23</sup> Institute of Space Sciences (ICE, CSIC) Campus UAB, Carrer de Can Magrans, s/n, E-08193, Bellaterra, Spain

<sup>24</sup> Institut d'Estudis Espacials de Catalunya (IEEC), C/Gran Capità, 2-4, E-08034, Barcelona, Spain

Received 2021 March 11; revised 2021 July 16; accepted 2021 July 27; published 2021 October 22

## Abstract

Giant stars as known exoplanet hosts are relatively rare due to the potential challenges in acquiring precision radial velocities and the small predicted transit depths. However, these giant host stars are also some of the brightest in the sky and so enable high signal-to-noise ratio follow-up measurements. Here, we report on new observations of the bright ( $V \sim 3.3$ ) giant star  $\iota$  Draconis ( $\iota$  Dra), known to host a planet in a highly eccentric  $\sim 511$  day period orbit. TESS observations of the star over 137 days reveal asteroseismic signatures, allowing us to constrain the stellar radius, mass, and age to  $\sim 2\%$ ,  $\sim 6\%$ , and  $\sim 28\%$ , respectively. We present the results of continued radial-velocity monitoring of the star using the Automated Planet Finder over several orbits of the planet. We provide more precise planet parameters of the known planet and, through the combination of our radial-velocity measurements with Hipparcos and Gaia astrometry, we discover an additional long-period companion with an orbital period of  $\sim 68^{+60}_{-36}$  yr. Mass predictions from our analysis place this substellar companion on the border of the planet and brown dwarf regimes. The bright nature of the star combined with the revised orbital architecture of the system provides an opportunity to study planetary orbital dynamics that evolve as the star moves into the giant phase of its evolution.

*Unified Astronomy Thesaurus concepts:* Photometry (1234); Radial velocity (1332); Exoplanet dynamics (490); Exoplanets (498); Exoplanet astronomy (486); Exoplanet systems (484); Exoplanet detection methods (489); Planet hosting stars (1242); Asteroseismology (73); Stellar astronomy (1583); Planetary dynamics (2173); Detection (1911)

*Supporting material:* machine-readable table

## 1. Introduction

Exoplanets have been discovered around a diversity of stellar types and with a broad range of orbital architectures (Ford 2014; Winn & Fabrycky 2015). Despite challenges with regards to stellar pulsations (Hatzes et al. 2018), radial-velocity (RV)

surveys for planets orbiting giant stars are underway (Hekker & Meléndez 2007; Reffert et al. 2015). One of the brightest and nearest giant stars known to host a planet is  $\iota$  Draconis (hereafter  $\iota$  Dra), a  $V = 3.29$  K2 giant star located at a distance of  $\sim 31$  pc. At the time of its detection by Frink et al. (2002),  $\iota$  Dra b, or HD 137759 b, was the first planet to be found to orbit a giant star. The initial detection, based on RV observations of a full planetary orbit, revealed an orbital period

<sup>25</sup> NSF Astronomy and Astrophysics Postdoctoral Fellow.

of  $\sim 536$  days, an eccentricity of 0.70, a minimum planet mass of  $8.9 M_J$ , and a semimajor axis of 1.3 au. These properties were refined by Zechmeister et al. (2008) with the help of an increased observational RV baseline and resulted in the detection of an additional linear trend in the residuals to the single-planet solution. The planet orbital properties were further refined by Kane et al. (2010), who confirmed the existence of the linear trend detection. To rule out the possibility of a stellar companion as the cause of the linear trend, Kane et al. (2014) investigated  $\iota$  Dra with the Differential Speckle Survey Instrument (DSSI) on the Gemini North telescope (Horch et al. 2009). These observations were able to exclude bound low-mass M dwarfs at wide separations. As the long-term linear trend continued, it became increasingly likely that it was caused by a substellar companion.

The potential of a transit event of the  $\iota$  Dra planet was evaluated in Kane et al. (2010). As planets orbiting giant stars tend to have large transit probabilities due to the size of the host stars (Assef et al. 2009) and planets with higher eccentricity also have an increased probability of transiting (Barnes 2007; Kane & von Braun 2008),  $\iota$  Dra b is expected to have a relatively high transit probability of  $\sim 16.5\%$  (Kane et al. 2010). In a recent study, Dalba et al. (2019) found  $\iota$  Dra had a  $11 \pm 3\%$  probability of having a transiting geometry, and subsequently a  $1.8 \pm 0.6\%$  probability of the Transiting Exoplanet Survey Satellite (TESS) seeing the transit in the primary mission.

Given the high dependence of transit probabilities and other planetary properties on the host star parameters, extracting reliable stellar properties is crucially important for continued studies of the system. Interferometric observations of  $\iota$  Dra by Baines et al. (2011) measured a stellar radius of  $\sim 12 R_\odot$  and an effective temperature of  $T_{\text{eff}} = 4545$  K. However, long-term and continuous precision photometry of the star is challenging due to its brightness and northern celestial location, restricting access from many facilities. Such a photometric data set would not only allow the possibility of transit detection, but enable a concise evaluation of the stellar properties via asteroseismology, which is particularly well suited to giant stars due to the large amplitudes and accessible frequencies available (Campante et al. 2016).

Here, we present a new analysis of the  $\iota$  Dra system that includes a substantially updated RV data set, Hipparcos and Gaia astrometry, and precision photometry from TESS. In particular, the combination of astrometry with the new RV data demonstrate that the linear trend has finally revealed a curvature, allowing an orbital period for the second companion to be estimated. In Section 2 we describe the new RV data, and our analysis of the photometry from TESS. We provide refined stellar properties in Section 3, including an analysis of the spectral energy distribution and an asteroseismic study enabled by the precision data from TESS. We present our revised orbital properties of  $\iota$  Dra b and of the long-term RV trend in Section 4, including a dynamical analysis with the MEGNO chaos indicator, orbital constraints on the outer companion from *The Joker*, and our best fit for the additional companion through the combination of RV and astrometry using *htof* and *orvara*. In Section 5 the orbital dynamics of planets in evolved systems are discussed, and conclusions and future directions are provided in Section 6.

**Table 1**  
Radial-velocity Observations of  $\iota$  Dra

Time BJD	RV $\text{m s}^{-1}$	Uncertainty $\text{m s}^{-1}$	Telescope
2458156.925	−194.377146	2.292272	apf
2458156.925	−202.796987	2.548035	apf
2458156.926	−196.984888	2.431443	apf
2458160.96	−229.261174	2.014732	apf
2458160.96	−226.650269	2.191855	apf
2458160.961	−229.033612	2.148611	apf
2458161.065	−217.703627	2.105308	apf
2458161.065	−219.498013	3.215146	apf
2458161.066	−218.682983	2.15082	apf
2458162.943	−231.747948	2.204404	apf

(This table is available in its entirety in machine-readable form.)

## 2. Observations

### 2.1. TESS Photometry

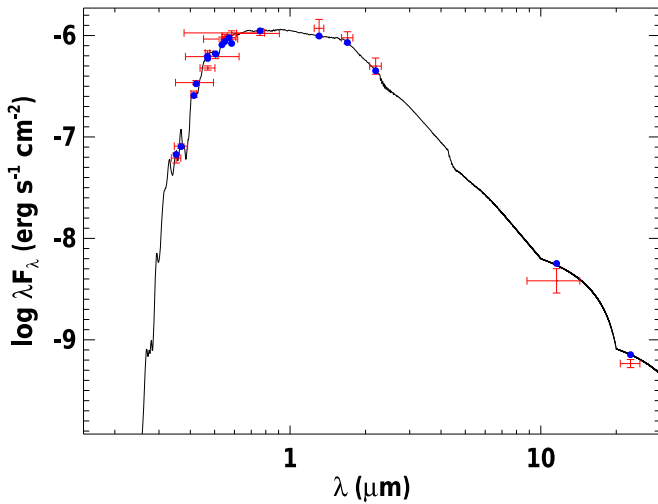
The TESS mission is designed to survey nearby F, G, K, and M type stars for signatures of transiting exoplanets (Ricker et al. 2015). TESS observations of  $\iota$  Dra occurred during Sectors 15, 16, 22, 23, and 24 at 2 minute cadence. At a magnitude of  $T_{\text{mag}} = 2.27$ ,  $\iota$  Dra is significantly saturated as seen by the TESS detector, and accordingly required special processing to obtain a high-quality light curve. In particular, with the large postage stamp, spatially varying background light is a major source of noise (Eisner et al. 2019; Dalba et al. 2020b), and to ameliorate this we create a spatially varying background model using a second-order polynomial fitted to pixels at the edge of the aperture. As well as this, the default aperture from the SPOC pipeline was too small, and we instead created our own: first we defined a threshold mask at 50% maximum amplitude using *lightkurve* (Lightkurve Collaboration et al. 2018), and applied a binary dilation to expand this by one pixel in each direction. The Jupyter notebook used to generate this light curve is available on GitHub: [https://github.com/hvidy/tessbkgd/blob/stable/notebooks/iot\\_Dra\\_tpf.ipynb](https://github.com/hvidy/tessbkgd/blob/stable/notebooks/iot_Dra_tpf.ipynb).

Upon inspection of the TESS photometry we found no indications of any transiting planets. However, none of the TESS observations of  $\iota$  Dra coincide with the expected time of conjunction for  $\iota$  Dra b, so a transit of this planet cannot be ruled out. Future observations of  $\iota$  Dra by TESS may coincide with the time of inferior conjunction of  $\iota$  Dra b. This is discussed further in Section 5.

### 2.2. Radial Velocities

A total of 165 RV observations obtained with the 0.6 m Coudé Auxiliary Telescope (CAT) and the Hamilton Échelle Spectrograph (HES) at the Lick Observatory in California were extracted from previous published works by Frink et al. (2002), Butler et al. (2006), Zechmeister et al. (2008), and Kane et al. (2010).

An additional 456 RV observations were obtained by the Levy spectrometer on the Automated Planet Finder (APF; Radovan et al. 2014; Vogt et al. 2014) at Lick Observatory from 2018 February to 2021 February. The spectra were reduced using the standard procedures of the California Planet Search (Howard et al. 2010). A subset of the APF RV data set is found in Table 1. The full data set will be made available in machine-readable form.



**Figure 1.** Spectral energy distribution of  $\iota$  Dra. Red symbols represent the observed photometric measurements, where the horizontal bars represent the effective width of the passband. Blue symbols are the model fluxes from the best-fit Kurucz atmosphere model (black).

### 3. Stellar Characterization

#### 3.1. Spectral Energy Distribution

As an independent determination of the basic stellar parameters, we performed an analysis of the broadband spectral energy distribution (SED) of the star together with the Gaia DR2 parallaxes (adjusted by  $+0.08$  mas to account for the systematic offset reported by Stassun & Torres 2018), in order to determine an empirical measurement of the stellar radius, following the procedures described in Stassun & Torres (2016) and Stassun et al. (2017, 2018a). We pulled the  $UBV$  magnitudes from Mermilliod (2006), the  $uvby$  Strömgren magnitudes from Paunzen (2015), the  $B_T V_T$  magnitudes from Tycho-2, the  $JHK_S$  magnitudes from 2MASS, the W3–W4 magnitudes from the Wide-field Infrared Survey Explorer (WISE), and the  $GG_{BP}GRP$  magnitudes from Gaia. Together, the available photometry spans the full stellar SED over the wavelength range  $0.3$ – $22 \mu\text{m}$  (see Figure 1).

We performed a fit using Kurucz stellar atmosphere models, with the effective temperature ( $T_{\text{eff}}$ ), metallicity ( $[\text{Fe}/\text{H}]$ ), and surface gravity ( $\log g$ ) adopted from the spectroscopic analysis of Jofré et al. (2015). The only additional free parameter is the extinction ( $A_V$ ), which we set to zero given the star’s proximity. The resulting fit is very good (Figure 1) with a reduced  $\chi^2$  of 2.8. Integrating the (unreddened) model SED gives the bolometric flux at Earth,  $F_{\text{bol}} = 1.692 \pm 0.059 \times 10^{-6} \text{ erg s}^{-1} \text{ cm}^{-2}$ . Taking the  $F_{\text{bol}}$  and  $T_{\text{eff}}$  together with the Gaia DR2 parallax gives the stellar radius,  $R_* = 11.94 \pm 0.32 R_\odot$ . In addition, we can use the  $R_*$  together with the spectroscopic  $\log g$  to obtain an empirical mass estimate of  $M_* = 1.72 \pm 0.29 M_\odot$ , which is roughly consistent with that estimated via the eclipsing-binary based empirical relations of Torres et al. (2010),  $M_* = 2.23 \pm 0.13 M_\odot$ . Finally, from the spectroscopic  $v \sin i$  together with  $R_*$  we obtain an estimate of the stellar rotation period lower limit,  $P_{\text{rot}} / \sin i = 325 \pm 78$  days.

#### 3.2. Asteroseismology

##### 3.2.1. Global Oscillation Parameters

Figure 2 shows the power spectrum of  $\iota$  Dra based on the full TESS light curve extracted in Section 2.1. It reveals a clear

power excess due to solar-like oscillations at  $\sim 40 \mu\text{Hz}$ . This is in agreement with Zechmeister et al. (2008), who measured solar-like oscillations with frequencies around  $34.7$ – $46.3 \mu\text{Hz}$ .

We started by measuring the large frequency separation,  $\Delta\nu$ , and the frequency of maximum oscillation amplitude,  $\nu_{\text{max}}$ , using a range of well-tested automated analysis methods (Huber et al. 2009; Mosser & Appourchaux 2009; Mathur et al. 2010; Corsaro & De Ridder 2014; Campante et al. 2017, 2019; García Saravia Ortiz de Montellano et al. 2018; Lightkurve Collaboration et al. 2018; Viani et al. 2019; Corsaro et al. 2020), which have previously been extensively applied to Kepler/K2 data. Returned values were subject to a preliminary step that involved the rejection of outliers following Peirce’s criterion (Peirce 1852; Gould 1855). A final, consolidated pair of values,  $\Delta\nu = 4.02 \pm 0.02 \mu\text{Hz}$  and  $\nu_{\text{max}} = 38.4 \pm 0.5 \mu\text{Hz}$ , then stem from the source/method (Huber et al. 2009) that minimizes the normalized rms deviation about the median. Uncertainties are the corresponding formal uncertainties.

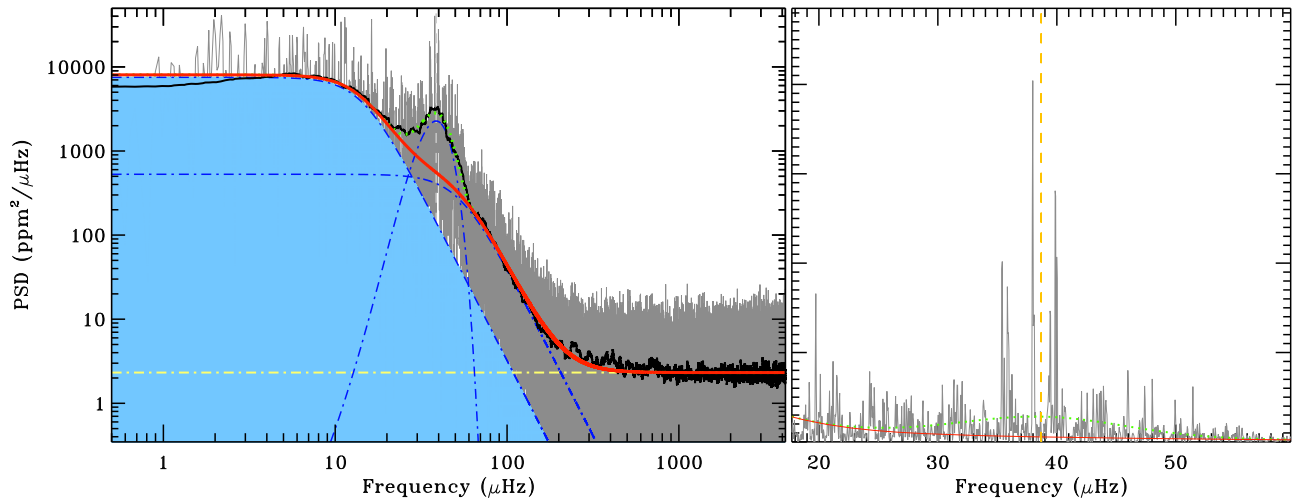
##### 3.2.2. Individual Mode Frequencies

A total of  $N = 7$  fitters extracted individual mode frequencies from the power spectrum. Methods employed ranged from an iterative sine-wave fitting approach (e.g., Lenz & Breger 2005; Bedding et al. 2010) to the fitting of Lorentzian and sinc<sup>2</sup> mode profiles (e.g., Handberg & Campante 2011; García Saravia Ortiz de Montellano et al. 2018; Corsaro et al. 2020). We then followed the procedure described in Campante et al. (2011) to produce two frequency lists, namely, a *minimal frequency list* and a *maximal frequency list*. The former includes modes (after outlier rejection) detected by more than  $\lfloor N/2 \rfloor$  fitters. One may think of it as a conservative list (16 modes). The latter includes modes (after outlier rejection) detected by at least 2 fitters (31 modes). The minimal list is thus a subset of the maximal list. Only those modes belonging to the minimal list will be effectively modeled in Section 3.2.4. Hereafter, we adopt a set of observed mode frequencies (and corresponding uncertainties) tracing back to a single fitter/method, namely, FAMED (Corsaro et al. 2020), so as to guarantee reproducibility. Table 5 lists all significant modes (i.e.,  $p_{\text{det}} \geq 0.993$ , see Section 5.3 of Corsaro et al. 2020 for details) returned by FAMED (note that not all modes belonging exclusively to the maximal list were found to be significant by FAMED and have thus not been listed). The dominant mode found by Zechmeister et al. (2008) coincides with the first mode listed in Table 5.

##### 3.2.3. Evolutionary State

Measurement of the period spacing between mixed modes allows distinguishing between hydrogen-shell burning (or red-giant branch; RGB) and helium-core burning (HeB) red giants (Bedding et al. 2011; Mosser et al. 2011). Estimation of the period spacing,  $\Delta\Pi_1$ , is, however, not possible when considering modes in the minimal list, owing to the limited number of observed dipole mixed modes per radial order. Use of the Vrard et al. (2016) method and evaluation of the asymptotic acoustic-mode offset (Kallinger et al. 2012; Christensen-Dalsgaard et al. 2014) also proved inconclusive.

We next resorted to machine-learning classification methods. We employed the deep learning method of Hon et al. (2017, 2018), which efficiently classifies the evolutionary state of oscillating red giants by recognizing visual features in their



**Figure 2.** Power spectrum of  $\iota$  Dra based on the full TESS light curve. Left panel: the power spectrum is shown in gray on a logarithmic scale (with a heavily smoothed version in black). The solid red curve is a fit to the background, consisting of two Harvey-like profiles (blue dotted–dashed curves) plus white noise (yellow, horizontal dotted–dashed line). A joint fit to the oscillation power excess (blue dotted–dashed Gaussian curve) and background is visible at  $\sim 40$   $\mu\text{Hz}$  as a dotted green curve. Right panel: the power spectrum is shown on a linear scale and centered on the oscillations. The vertical yellow dashed line is a proxy for  $\nu_{\text{max}}$ . The remaining curves have the same meaning as in the left panel.

power spectra. Application of this method points toward an RGB classification with high confidence ( $p > 0.9$ ). Alternatively, we made use of the `Clumpiness` evolutionary state classifier (Kuszlewicz et al. 2020), which returned a probability of  $\sim 0.8$  (when applied to the full TESS light curve) of the star being on the RGB.

### 3.2.4. Detailed Stellar Modeling

We modeled the modes in the minimal list, together with a set of classical constraints (namely,  $T_{\text{eff}}$ ,  $[\text{Fe}/\text{H}]$ , and  $L_*$ ; see Table 2), following the methodology of Li et al. (2020), without considering interpolation and setting the model systematic uncertainty to zero. The underlying grid of stellar models is described in Appendix B. Figure 3 is an échelle diagram showing the frequency match for a representative best-fitting model in the grid. We note that only RGB models were able to provide a sensible fit to the observed frequencies within the quoted  $T_{\text{eff}}$ ,  $[\text{Fe}/\text{H}]$ , and  $L_*$  ranges (we used  $5\sigma$  ranges). This constitutes further evidence in support of the RGB classification.

We provide values from detailed modeling for the stellar mass ( $M_*$ ), radius ( $R_*$ ), surface gravity ( $\log g$ ), and age ( $t$ ) in Table 2. Quoted uncertainties include both a statistical and a systematic contribution. The latter accounts for the impact of using different model grids—covering a range of input physics—and analysis methodologies on the final estimates, full details of which will be presented in a follow-up paper (T. Campante et al. 2021, in preparation). We note the excellent agreement (within  $1\sigma$ ) between the seismic and interferometric radii.

## 4. Detection of a Long-period Companion

### 4.1. Radial-velocity Analysis

The RV data for  $\iota$  Dra were fit using the RV modeling toolkit `RadVel` (Fulton et al. 2018) in order to refine the orbital solution and look for curvature within the previously reported linear trend to determine if there were indications for additional planetary companions. `RadVel` enables users to model Keplerian orbits in radial-velocity time series. `RadVel` fits RVs using an iterative

**Table 2**  
Stellar Parameters

Parameter	Value	Source
Basic Properties		
Gaia ID	DR2 1614731957530945280	1
TIC	165722603	2
TESS Mag.	2.27	2
Sp. Type	K2 III	3
Spectroscopy		
$T_{\text{eff}}$ (K)	$4504 \pm 62^a$	4
$[\text{Fe}/\text{H}]$ (dex)	$0.03 \pm 0.08^a$	4
$\log g$ (cgs)	$2.52 \pm 0.07$	4
SED & Gaia DR2 Parallax		
$F_{\text{bol}}$ ( $\text{erg s}^{-1} \text{cm}^{-2}$ )	$(1.692 \pm 0.059) \times 10^{-6}$	5
$R_*$ ( $R_{\odot}$ )	$11.94 \pm 0.32$	5
$L_*$ ( $L_{\odot}$ )	$52.78 \pm 2.10^b$	5
$\pi$ (mas)	$31.65 \pm 0.30^c$	1
Asteroseismology		
$\Delta\nu$ ( $\mu\text{Hz}$ )	$4.02 \pm 0.02$	5
$\nu_{\text{max}}$ ( $\mu\text{Hz}$ )	$38.4 \pm 0.5$	5
$M_*$ ( $M_{\odot}$ )	$1.54 \pm 0.09^d$	5
$R_*$ ( $R_{\odot}$ )	$11.79 \pm 0.24^d$	5
$\log g$ (cgs)	$2.48 \pm 0.01^d$	5
$t$ (Gyr)	$2.65 \pm 0.74^d$	5

#### Notes.

<sup>a</sup> Formal uncertainties have been inflated according to Torres et al. (2012).

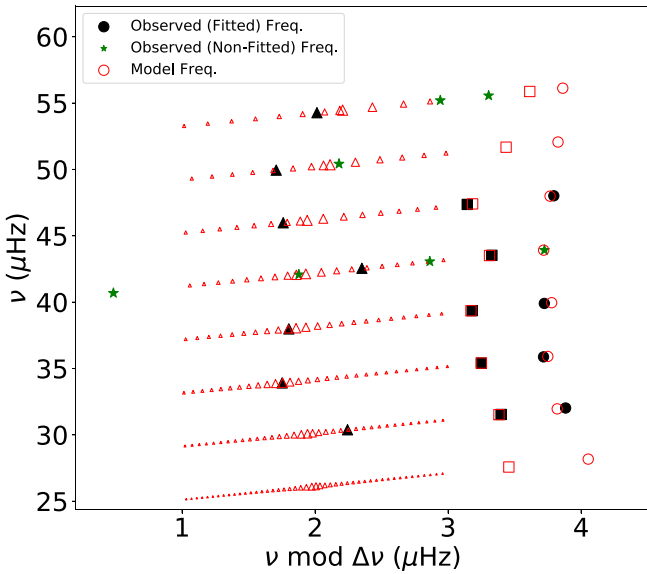
<sup>b</sup> Based on SED fit (Section 3.1) and Gaia DR2 parallax.

<sup>c</sup> Adjusted for the systematic offset of Stassun & Torres (2018).

<sup>d</sup> Uncertainties include both a statistical and a systematic contribution (added in quadrature).

**References.** (1) Gaia Collaboration et al. (2018), (2) Stassun et al. (2018b), (3) Keenan & McNeil (1989), (4) Jofré et al. (2015), (5) this work.

approach to solve the set of equations for the Keplerian orbit to determine the best fit for the observed RV curve. It then employs modern Markov Chain Monte Carlo (MCMC) sampling techniques (Metropolis et al. 1953; Hastings 1970; Foreman-Mackey et al. 2013) and robust convergence criteria to ensure accurately estimated orbital parameters and their associated uncertainties. Once the MCMC chains are well mixed, `RadVel`



**Figure 3.** Échelle diagram displaying the observed frequencies as well as the model frequencies corresponding to a representative best-fitting model (no interpolation was used and so this corresponds to a specific model in the grid). Filled black symbols represent observed (fitted) frequencies, i.e., belonging to the minimal list. Open red symbols are model frequencies. Circles, triangles, and squares indicate modes of angular degree  $\ell = 0$  (radial modes),  $\ell = 1$  (dipole modes), and  $\ell = 2$  (quadrupole modes), respectively. Green five-pointed stars correspond to observed frequencies not in the minimal list. The extra  $\ell = 2$  model frequencies correspond to the most p-like modes, whereas we have plotted a range of g-dominated  $\ell = 1$  model frequencies per order (with symbol size scaled as  $I^{-0.5}$ ,  $I$  being the mode inertia).

then supplies an output of the final parameter values from the Maximum A Posteriori (MAP) fit.

We used the previously published orbital values from Butler et al. (2006) as priors for  $\iota$  Dra b and allowed all orbital parameters, including the linear and curvature terms, to be free. The best-fit solution from RadVel gave  $\iota$  Dra b an orbital period of  $510.855 \pm 0.014$  days, a semi-amplitude of  $311 \pm 1 \text{ m s}^{-1}$ , eccentricity  $0.7008 \pm 0.0018$ , and using our  $M_*$  value from Table 2, a derived  $M_p \sin i$  of  $11.67 \pm 0.45 M_J$ . The central 68% confidence intervals computed from the MCMC chains are presented in Table 3. The preferred model includes linear and curvature terms for  $\iota$  Dra. This indicates an additional body in orbit around  $\iota$  Dra. The residuals of the single-planet model can be seen to flatten out, indicating the additional orbiting body has reached quadrature (Figure 4).

Using the iterative periodogram algorithm RVSearch (L. J. Rosenthal 2021, et al. in preparation), we searched for the period of the companion. RVSearch works by first defining the orbital frequency/period grid over which to search, with sampling such that the difference in frequency between adjacent grid points is  $\frac{1}{2\pi\tau}$ , where  $\tau$  is the observational baseline. Using this grid, a goodness-of-fit periodogram was computed by fitting a sinusoid with a fixed period to the data for each period in the grid. The goodness-of-fit was measured as the change in the Bayesian Information Criterion (BIC) at each grid point between the best-fit one-planet model with the given fixed period, and the BIC value of the zero-planet fit to the data. A power law was then fit to the noise histogram (50%–95%) of the data and accordingly a BIC detection threshold corresponding to an empirical false-alarm probability of 0.0003 was extrapolated. If one planet was detected, a final fit to the one-planet model with all parameters free was completed, and the BIC of that best-fit model recorded. Then a

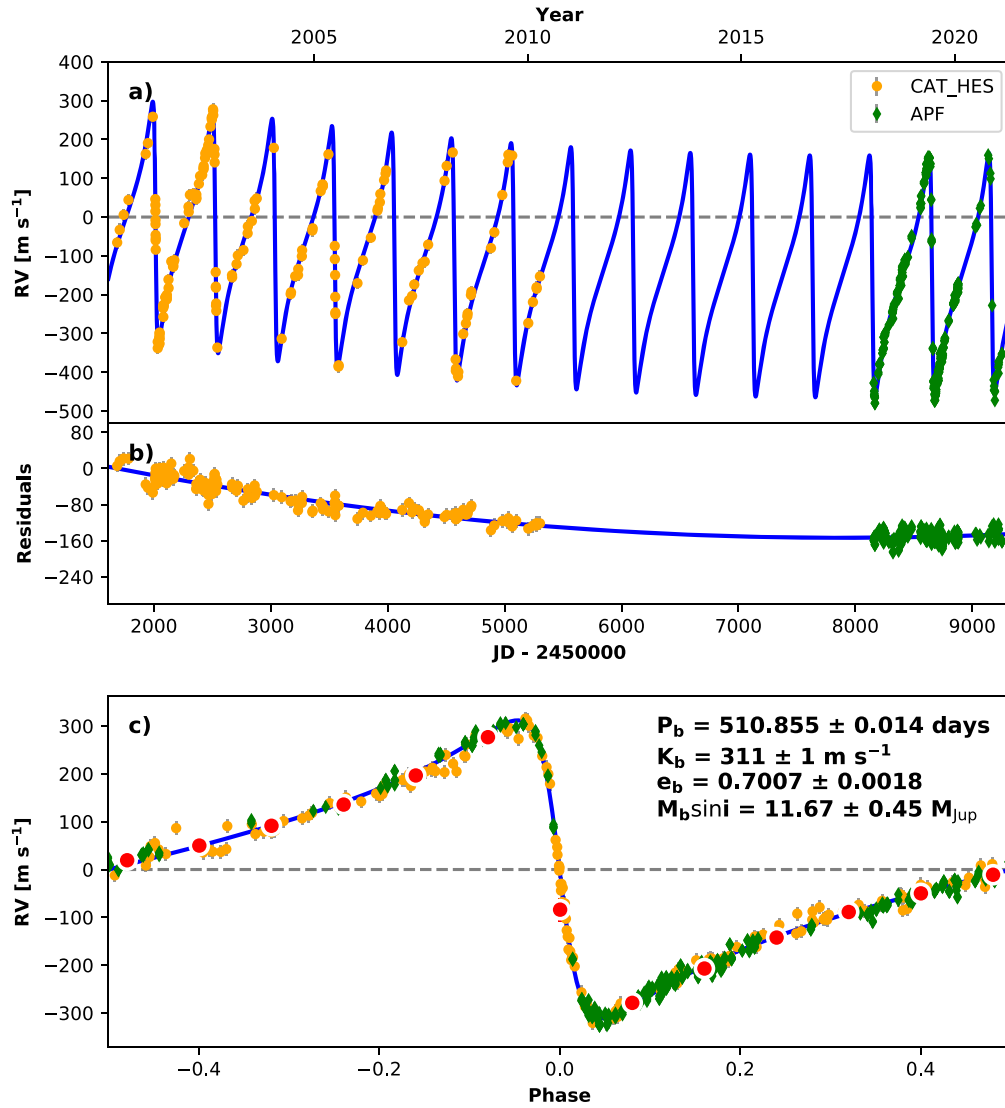
**Table 3**  
RadVel MCMC Posteriors for  $\iota$  Dra b

Parameter	Credible Interval	Units
<b>Orbital Parameters</b>		
Orbital Period $P$	$510.855 \pm 0.014$	days
Time of Inferior Conjunction $T_{\text{conj}}$	$2452014.2 \pm 0.13$	JD
Time of Periastron $T_{\text{peri}}$	$2452014.19 \pm 0.16$	JD
Eccentricity $e$	$0.7008 \pm 0.0018$	
Argument of Periastris $\omega$	$1.5696 \pm 0.0056$	radians
Velocity Semi-amplitude $K$	$311 \pm 1$	$\text{m s}^{-1}$
<b>Other Parameters</b>		
Mean Center-of-mass Velocity $\gamma_{\text{apf}}$	$\equiv 226.3573$	$\text{m s}^{-1}$
Mean Center-of-mass Velocity $\gamma_{\text{CATHES}}$	$\equiv 74.8982$	$\text{m s}^{-1}$
Linear Acceleration $\dot{\gamma}$	$-0.05 \pm 0.0017$	$\text{m s}^{-1} \text{ d}^{-1}$
Curvature $\ddot{\gamma}$	$4.14e-06 \pm 2.5e-07$	$\text{m s}^{-1} \text{ d}^{-2}$
Jitter $\sigma_{\text{apf}}$	$10.67^{+0.44}_{-0.42}$	$\text{m s}^{-1}$
Jitter $\sigma_{\text{CATHES}}$	$13.85^{+0.92}_{-0.84}$	$\text{m s}^{-1}$
<b>Derived Posteriors</b>		
Mass $M_p \sin i$	$11.67^{+0.45}_{-0.46}$	$M_{\text{Jup}}$
Semimajor Axis $a$	$1.448^{+0.028}_{-0.029}$	au

second planet was added to the RV model and another grid search was conducted, leaving the parameters of the first planet free to converge to a more optimal solution. In this case the goodness-of-fit was computed as the difference between the BIC of the best-fit one-planet model, and the BIC of the two-planet model at each fixed period in the grid. The detection threshold was set in the manner described above and this iterative search continued until the  $n + 1$ th search ruled out additional signals. For  $\iota$  Dra one significant companion signal was detected by the algorithm. The periodogram resulting from this analysis is shown in Figure 5 panel (f). The horizontal dotted line indicates a false-alarm probability (FAP) threshold of 0.001 (0.1%). The vertical red dashed line shows the location of a common alias caused by the Earth’s orbital (annual) motions. Panel (e) shows the best fit of the signal with an estimated period of  $\sim 45,594$  days, eccentricity of  $\sim 0.4$ , semi-amplitude of  $\sim 420 \text{ m s}^{-1}$  and  $M_p \sin i$  of  $\sim 38 M_{\text{Jup}}$ . This detection is beyond the baseline of the RV data and so there is a large uncertainty associated with this period. To refine the parameter space of the companion we run both a dynamical analysis with MEGNO and then further constrain the orbits with The Joker.

#### 4.2. Dynamical Analysis With MEGNO

To constrain the parameter space of the additional orbiting body, we performed a dynamical simulation using the MEGNO (Mean Exponential Growth of Nearby Orbits) chaos indicator (Cincotta & Simó 2000) to determine the range of semimajor axis and eccentricity configurations that this second body could have. The MEGNO simulation was carried out within the  $N$ -body package REBOUND (Rein & Liu 2012) with the symplectic integrator WHFast (Rein & Tamayo 2015). For planetary systems, the MEGNO indicator is useful in distinguishing the quasi-periodic or chaotic orbital time evolution of planetary bodies within the system (Hinse et al. 2010), where a chaotic state for a planet is less likely to maintain long-term orbital stability. For our simulation, we explored the possible orbital configurations of this potential outer companion by varying its semimajor axis and eccentricity value. The range of semimajor



**Figure 4.** (a) Best-fit single-planet Keplerian orbital model for  $\iota$  Dra. Yellow data points were taken using the Coudé Auxiliary Telescope with the Hamilton Échelle Spectrograph (CAT\_HES) and green were taken using the Automated Planet Finder (APF) with the Levy spectrometer. The maximum-likelihood model is plotted. The thin blue line is the best-fit model. (b) Residuals to the best-fit one-planet model. The curvature of the residuals has flattened out, indicating that this system is turning around. (c) RVs phase-folded to the ephemeris of planet b. The small point colors and symbols are the same as in panel (a). Red circles are the same velocities binned in 0.08 units of orbital phase. The phase-folded model for planet b is shown as the blue line. See Table 3 for the definition of the orbital parameters shown in panel (c).

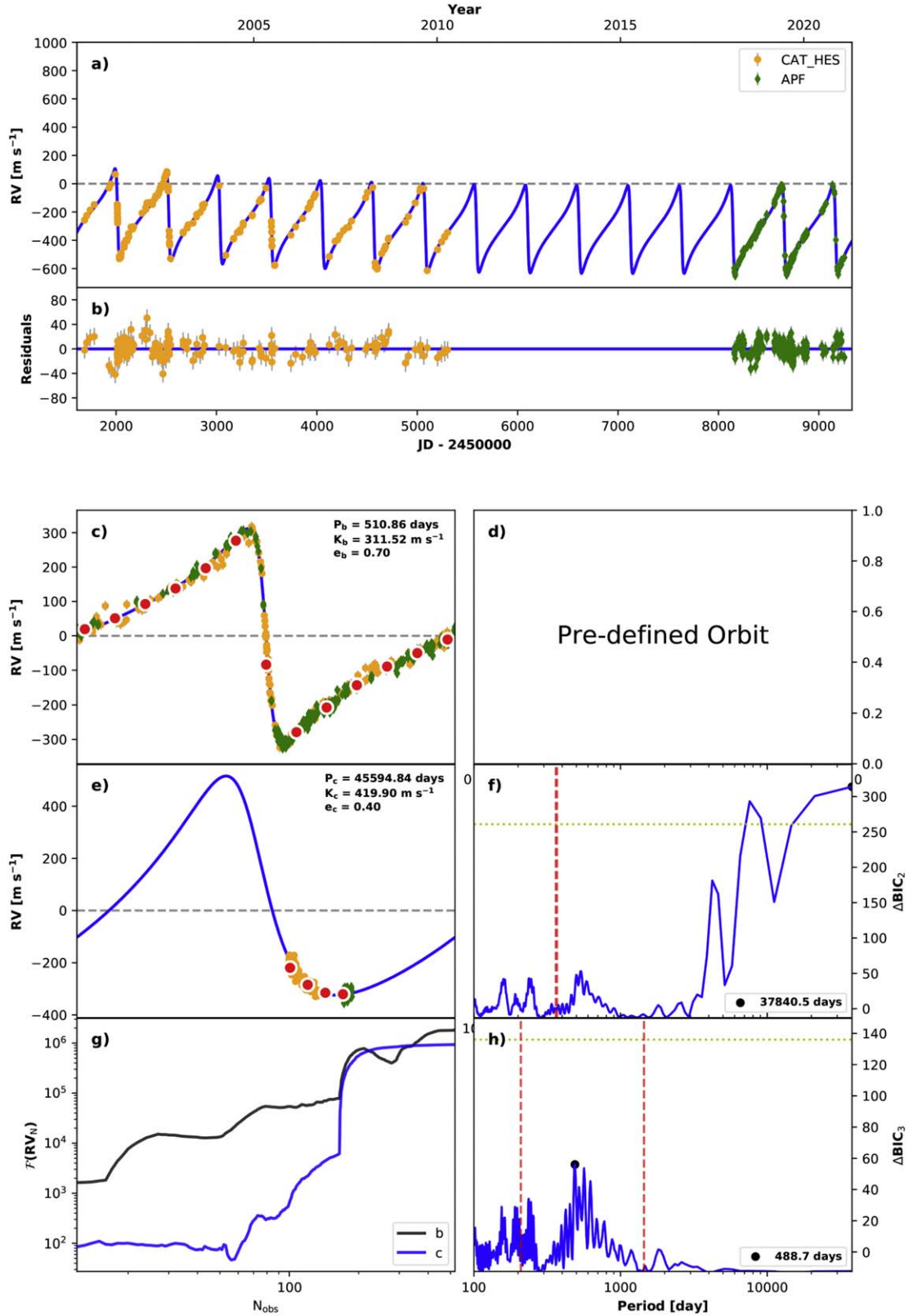
axis was tested between 8 and 40 au and for eccentricity, we tested a range from 0 and 0.75. The lower limit of the semimajor axis is provided by the baseline of observations, as a full orbit has not been completed. The upper limit of eccentricity was provided by the initial JOKER fit (see Section 4.3). The mass of the outer orbiting body was assumed to be 38 Jupiter masses ( $M_{\text{Jup}}$ ). All bodies were assumed to be co-planar with an edge-on inclination and the outer companion was assigned an argument of periastron value of  $326^\circ$  derived from the JOKER fit. The MEGNO simulation was run for each grid point for 20 million years integration time with a time step of 0.035 yr ( $\sim 13$  days). The time step is equivalent to 1/40 the orbital period of planet b, and is half of the recommended time step (Duncan et al. 1998) to ensure enough sampling when the highly eccentric planet b passes through periastron.

Shown in Figure 6 is the result of the simulation. The horizontal and vertical axes represent the range of semimajor axis and eccentricity that we tested. Each grid is color coded based on the

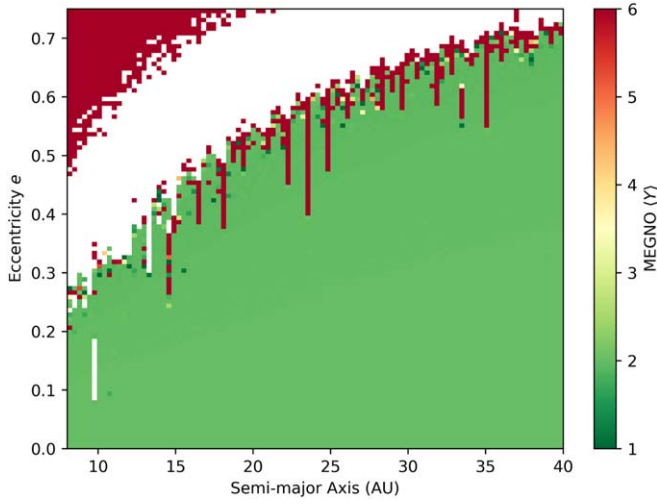
final MEGNO value for that specific configuration, where a MEGNO value around 2 (green) indicates nonchaotic results and planets all undergo quasi-periodic motion. Higher MEGNO values represented by warmer colors indicate chaos results for the system, and early termination with NaN MEGNO values caused by irregular events such as close encounters and collisions are marked in white. Locations with MEGNO values far from 2 are not favorable locations for the potential outer companion. The simulation indicates that the system would be unlikely to be in a chaotic state if the outer companion orbits close to the lower limit of semimajor axis with a low eccentricity. But other configurations with higher eccentricities become available at larger orbital separations, except several locations indicated by the white or red vertical bars where resonances may exist.

#### 4.3. Further Constraints On Outer Companion

To further refine the parameter space, we used The Joker (Price-Whelan et al. 2017) to predict orbital solutions for the



**Figure 5.** RVSearch results. Panels (a), (b), and (c) show the known fit from Figure 4. Panel (e) shows the best fit of the new planet signal orbiting  $\iota$  Dra with an estimated period of 45,594.84 days. Panel (f) shows the periodogram with a signal at  $\sim 37,840.5$  days. The horizontal dotted line indicates a false-alarm probability (FAP) threshold of 0.001 (0.1%). The vertical dashed line shows the location of a common alias caused by the Earth's orbital (annual) motions. Note the wide peak indicates a large uncertainty on the period of this signal. More data is needed to refine the orbital parameters of this additional planet. Panel (g) and Panel (h) show the running periodogram and the results from the residuals. The highest peak at 488.7 days does not exceed the FAP threshold of 0.001 and so it is concluded that there are no further significant periodic signals present in the data.



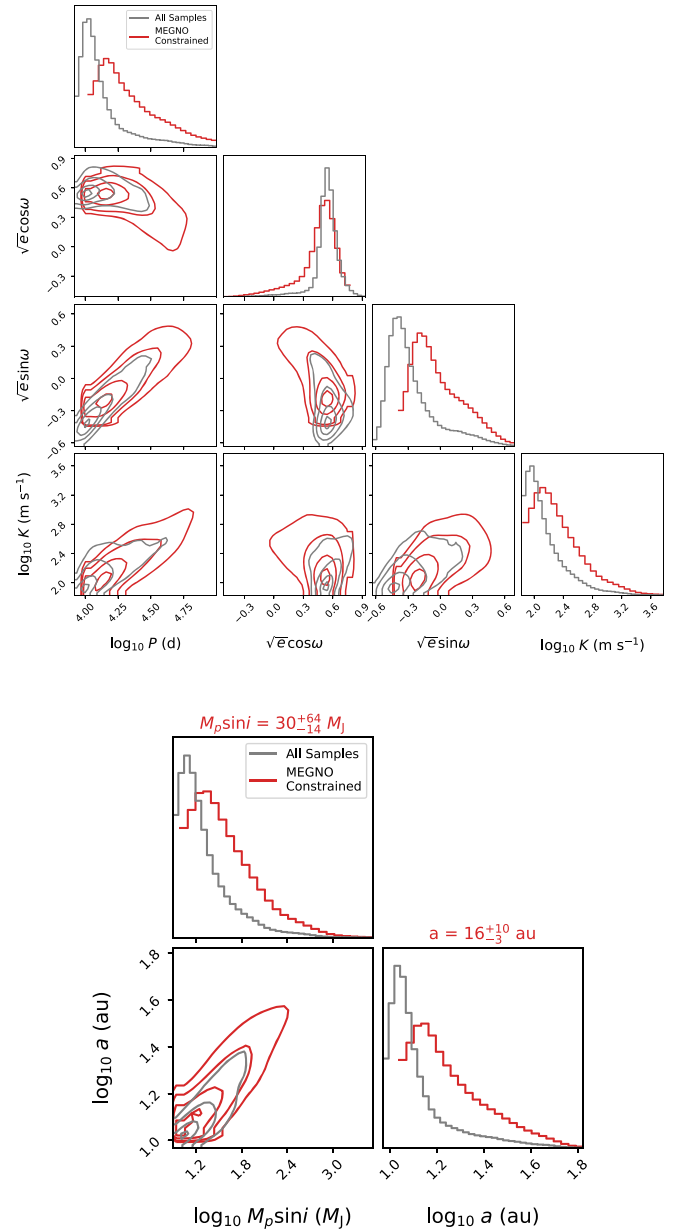
**Figure 6.** MEGNO simulation result showing the possible orbital configurations of the potential outer companion. Grids in green with value around 2 indicate nonchaotic results and are dynamically viable locations. Grids in other colors represent chaos and are not favorable locations for the outer companion. Areas in white indicate NaN MEGNO values where early termination was caused by irregular events such as close encounters and/or collisions.

additional body. The *Joker* is a Monte Carlo sampler that employs von Neumann rejection sampling to model RV variations for two-body systems (Price-Whelan et al. 2017). Our interest in constraining the orbital properties of the outer companion required us to first remove the signal of the inner planet from the RV observations. We subtracted the maximum-likelihood fit from the *Radvel* analysis (Section 4.1) but did not include the fitted values of acceleration (linear trend and/or curvature). This left a time series of RVs that contained only the trend from the outer companion.

In fitting these RV data with *The Joker*, we applied the default priors. The companion orbital period was assumed to be log-normal between 7500 days (roughly the baseline of observations) and 100,000 days. The prior over the companion eccentricity was a Beta distribution with shape parameters  $\alpha = 0.867$  and  $\beta = 3.03$ , which describes the known exoplanet samples at long orbital periods (Kipping 2013). The argument and phase of periastron as well as the semi-amplitude and systemic velocity all had uniform, noninformative priors. Lastly, we fixed the RV jitter to the value derived in the *Radvel* analysis (Section 4.1).

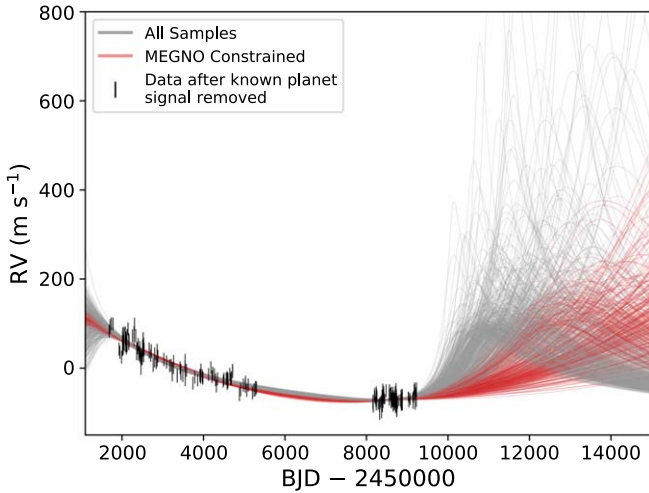
Using *The Joker*, we made  $2^{30}$  ( $\sim 1.1 \times 10^9$ ) draws from the prior distributions, of which 8912 survived. We show the posteriors comprised of the surviving samples in Figure 7. The posterior for companion orbital period peaks near 10,000 days but has a long, low-probability tail out to longer values. We found that this tail continued out to whatever maximum period value we chose, which was not surprising given that small fraction of the orbit our data cover. The shorter-period solutions generally required higher eccentricity whereas longer-period solutions defaulted to the prior and were more circular. Companion minimum mass peaked around  $11 M_{\text{Jup}}$  but also had a long, low-probability tail to higher values.

So far, our analysis has not considered the constraints derived by the MEGNO analysis. However, as shown in Figure 6, this simulation provides a constraint in eccentricity–semimajor axis space. There is an *envelope* of low MEGNO  $\langle Y \rangle$  values that favor lower eccentricity, larger orbits. We approximated this envelope as the interface between the white



**Figure 7.** Top: The *Joker* fitted posteriors. Bottom: derived posteriors for mass ( $M_p \sin i$ ) and semimajor axis ( $a$ ). Gray posteriors are results from *The Joker* without constraints from the MEGNO analysis. Red posteriors include constraints from the MEGNO analysis. The inclusion of the MEGNO constraints resulted in the removal many of the shorter-period, highly eccentric solutions. The orbital period, semimajor axis, minimum companion mass, and semi-amplitude were all pushed toward higher values. In particular, the minimum mass moved from the planetary mass regime and into the brown dwarf regime.

and red/green regions in Figure 6 and used it to divide the posteriors from *The Joker*. This kind of analysis has been employed previously to interpret results from *The Joker* in combination with additional limiting information (Dalba et al. 2020a). The resulting posteriors are overplotted on those for all surviving draws in Figure 7. The primary effect of including the chaos indicator results is to remove many of the shorter-period, highly eccentric solutions. This pushes the orbital period, semimajor axis, minimum companion mass, and semi-amplitude all toward higher values. Specifically, the minimum companion mass moves out of the planetary mass regime and into the brown dwarf (or substellar) regime.



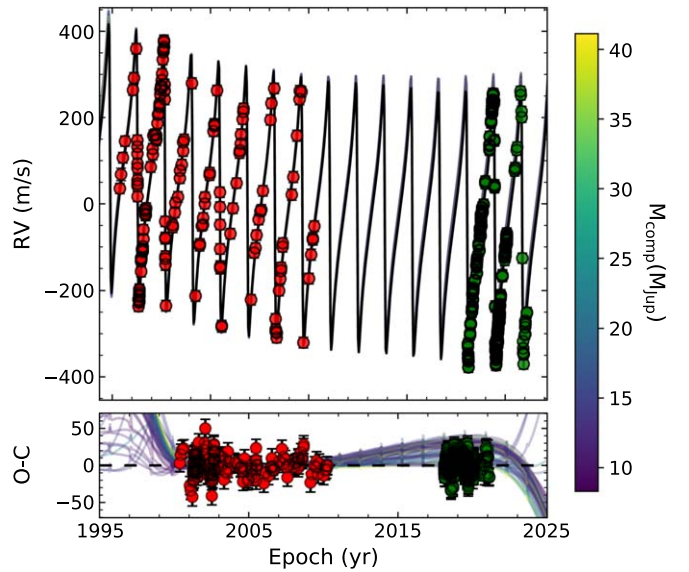
**Figure 8.** A representative subset of the surviving *The Joker* orbits. The orbits are a draw of  $\sim 10\%$  of the full set of surviving draws. Black vertical lines represent the time series RV data after the subtraction of the known planet signal. The gray curves represent orbital solutions that do not consider the MEGNO constraints, red curves are those that include the MEGNO constraints. Inclusion of the MEGNO analysis pushes the orbits to longer period, less eccentric solutions.

In Figure 8, we display a representative subset of the orbits corresponding to the surviving posterior draws. We also show the time series RV observations after the subtraction of the known planet signal. The gray curves, which do not consider the MEGNO constraints, are noticeably more eccentric and shorter period than the red curves, which are consistent with the MEGNO analysis.

#### 4.4. Combined Radial-velocity and Astrometry Analysis

By combining absolute astrometry with RV, the true motion of the star can be observed and planet mass and orbital parameters further constrained. RV measurements probe the line-of-sight acceleration while absolute astrometry measures the orthogonal component. For  $\iota$  Dra c, the RV curvature sets a lower limit on the mass, while the lack of a significant acceleration in the absolute astrometry provides an upper limit. We used *orvara*, an open-source Python package created by Brandt et al. (2021; details found therein) that performs a comprehensive joint MCMC analysis to determine orbital fits for planetary (or binary star) systems using a combination of Hipparcos (ESA Special Publication 1997; van Leeuwen 2007) and Gaia (Gaia Collaboration et al. 2016, 2018, 2021) astrometry, RV, and/or relative astrometry.

The RV data along with absolute astrometry from Gaia and Hipparcos was fit by *orvara* and the best-fit solution is shown in Figure 9. The top panel shows the RV observations from the Lick Observatory CAT with the HES in red and the APF in green, with the thick black line showing the highest likelihood orbital solution. The bottom panel represents the corresponding Observed–Calculated (O–C) residuals. The O–C residuals indicate the deviation of the observed value from the most likely orbit. The bottom panel also includes 50 colored lines. These represent 50 orbits chosen randomly from the posterior probability distribution, the colors corresponding to the mass of the companion ( $M_{\text{comp}}$ ) as indicated by the color bar on the right. The preferred fit by *orvara* agrees with the RadVel solution of  $\iota$  Dra b in Section 4.1, including the  $M_p \sin i$  value of  $11.82^{+0.42}_{-0.41}$ , which agrees with the RadVel estimate in Table 3. As both

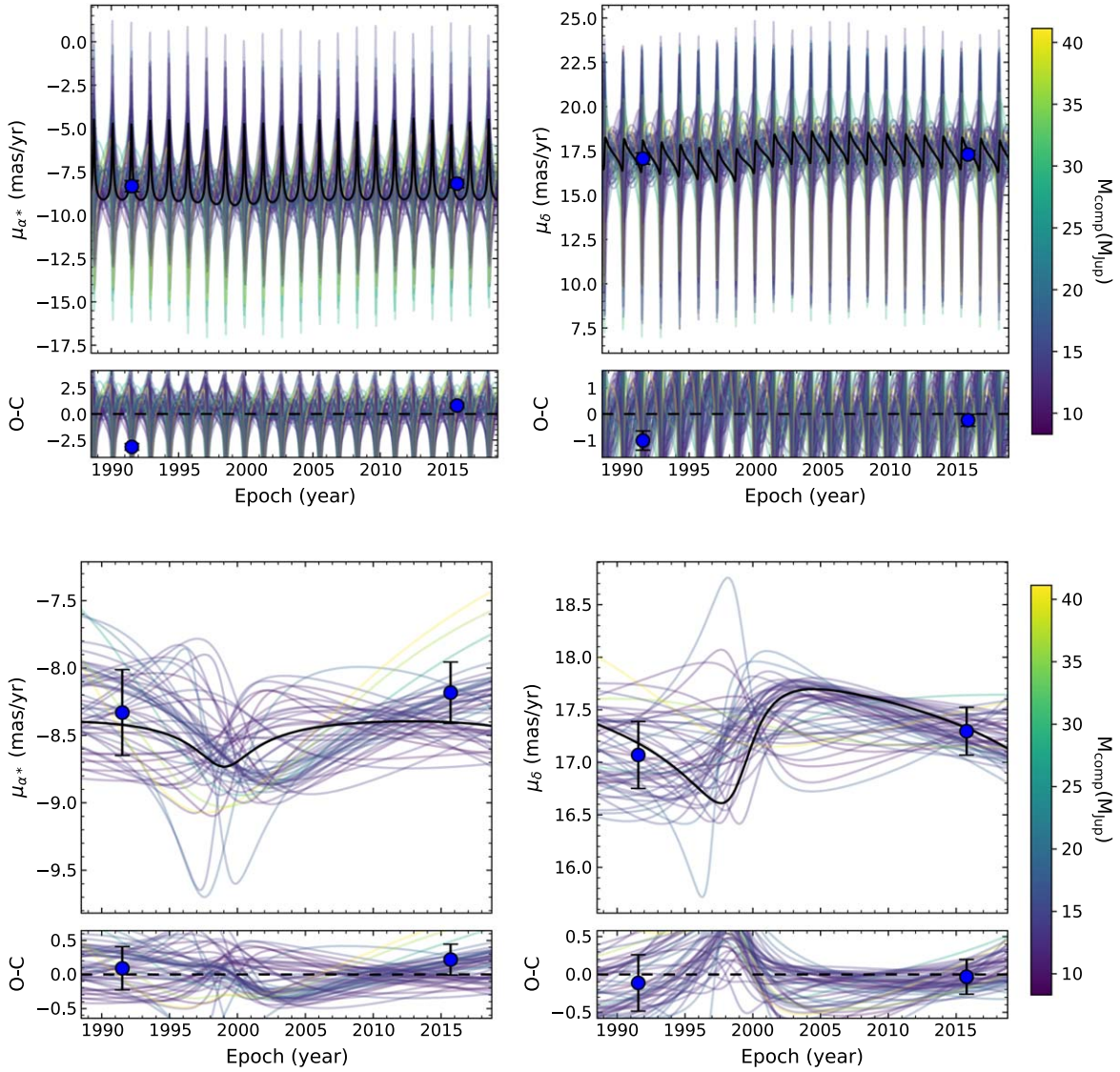


**Figure 9.** *orvara* fit of the  $\iota$  Dra system. Data points in red are those from the Coudé Auxiliary Telescope (CAT) with the Hamilton Echelle Spectrograph (HES); those in green were taken using the Automated Planet Finder (APF) with the Levy spectrograph. The thick black line shows the highest likelihood orbital solution. The fit produced by *orvara* agrees with the RadVel fit shown in Figure 4. The bottom panel shows the observed–calculated (O–C) residuals, along with colored lines indicating 50 random orbits from the posterior probability distribution. The color bar on the right of the plot indicates the mass of the outer companion ( $M_{\text{comp}}$ ) that each of these colors represent.

Hipparcos and Gaia fits to the proper motions of stars are integrated over each instrument’s mission baseline ( $\sim 3.5$  yr for Hipparcos, and 34 months for Gaia EDR3), rather than measuring instantaneous proper motions, astrometry with these instruments is not sensitive to planets with periods shorter than this baseline, like  $\iota$  Dra b. For this reason it is expected that the result from *orvara* for the inner planet would agree with the RadVel solution. Astrometry is, however, extremely useful when fitting a long-period object like the outer companion.

*orvara* uses the Hundred Thousand Orbit Fitter (*htof*, Brandt et al. submitted) to fit the proper motion of a star. *htof* computes synthetic Hipparcos and Gaia catalog positions and proper motions and then compares this to the absolute astrometry from the Hipparcos–Gaia Catalog of Accelerations (HGCA; Brandt 2018, 2021). We used the EDR3 version of the HGCA for  $\iota$  Dra. The proper motion of the  $\iota$  Dra system in R.A. ( $\mu_{\alpha^*}$ ) and decl. ( $\mu_{\delta}$ ) due to both companions, and also from just the outer companion, are in Figure 10. Again, the black line represents the best-fit orbit in the MCMC chain, whereas the other colored lines represent 50 random draws with masses corresponding to the color bars on the right. Due to the integration period of both Gaia and Hipparcos exceeding the period of  $\iota$  Dra b, little information is gained by including the proper-motion analysis for this planet, as can be seen in the top panels of Figure 10. The bottom panels, showing the proper motion of  $\iota$  Dra due to the outer companion, are much more informative and show the orbital constraints determined from the inclusion of proper motion for this object clearly. Note that the mean proper motion was used to compute the MCMC chain, but is not shown in the proper-motion plots. It is a constraint on the integrated proper motion between  $\approx 1991$  and  $\approx 2016$ .

The result of our comprehensive joint MCMC analysis of the RV and astrometric data is presented in the corner plot of



**Figure 10.** *orvara* proper motion of  $\iota$  Dra due to both companions (top) and due to just the outer companion (bottom), in R.A. ( $\mu_{\alpha^*}$ ) on the left and decl. ( $\mu_{\delta}$ ) on the right. The black line represents the best-fit orbit in the MCMC chain, whereas the other lines represent 50 random draws. The color bar on the right indicates the outer companion mass ( $M_{\text{comp}}$ ) for each orbital draw. The lower panels of each run represent the Observed–Calculated (O–C) residual.

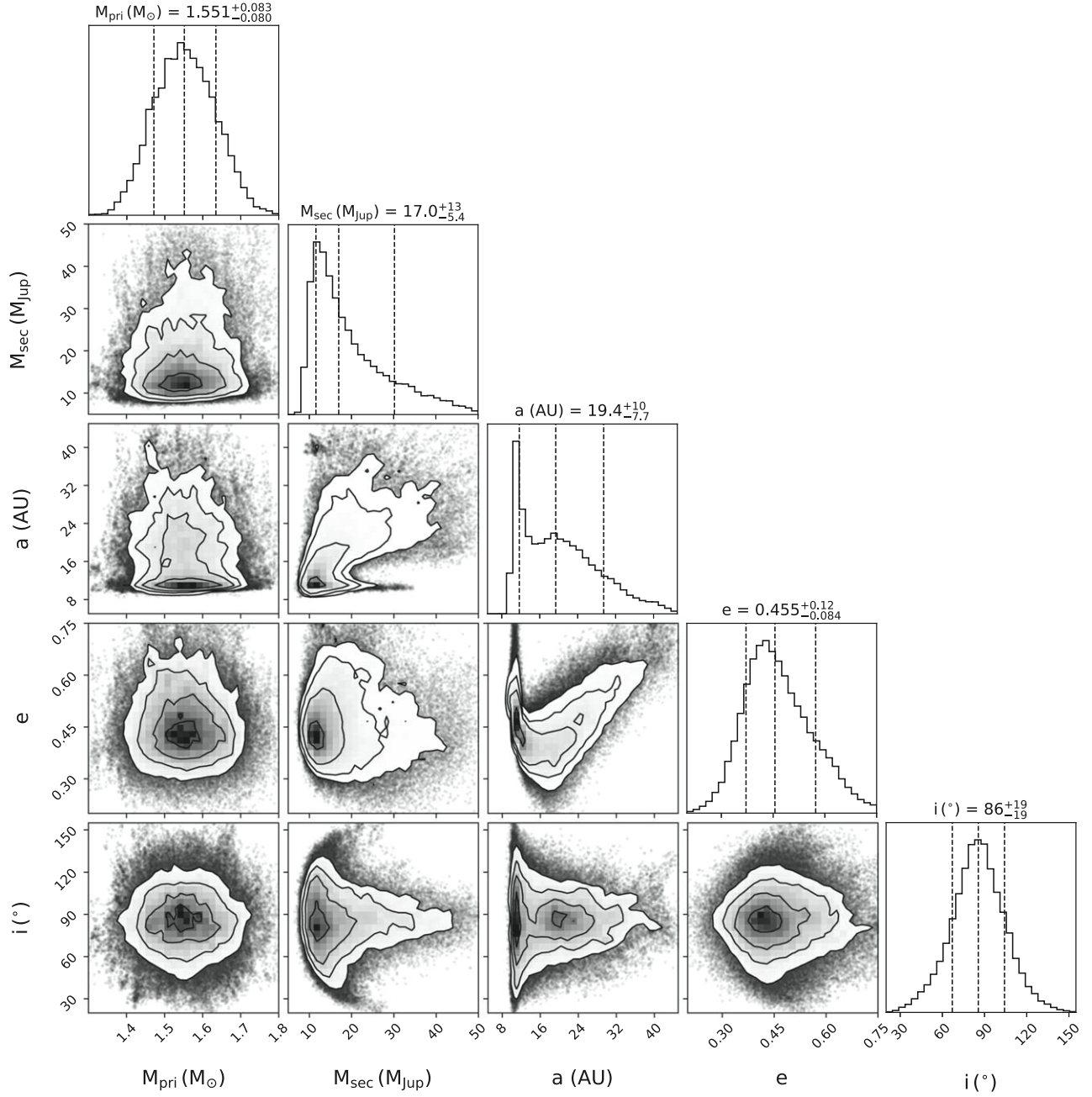
Figure 11 and Table 4. This includes derived posterior probabilities for the outer companion’s semimajor axis  $a$ , eccentricity  $e$ , inclination  $i$ , mass  $M_s$ , and the mass of the primary star  $M_{\text{pri}}$ . Rather than using the default priors of  $1/M_s$  and  $1/a$  for the companion mass and semimajor axis respectively, we use uniform priors for each to avoid causing a bias to low-mass and low semimajor axis solutions. The preferred solution from *orvara* gives the outer companion a mass of  $17.0^{+13}_{-5.4} M_{\text{Jup}}$ . This puts the outer companion on the border of the planet and brown dwarf regimes. This mass estimate agrees with the predicted mass from The Joker analysis in Section 4.3 and confirms that the outer companion is a substellar object.

## 5. Discussion

Stellar evolution can have an important impact on the dynamical evolution of the planets in a system (Jones et al. 2014; Damiani & Mathis 2018; Grunblatt et al. 2019), including planets that lie within a dramatically evolving Habitable Zone

(Gallet et al. 2017; Farr et al. 2018). The discovery of planets in eccentric orbits around evolved stars is critically important for diagnosing the source of such eccentricities (Wittenmyer et al. 2017; Grunblatt et al. 2018; Bergmann et al. 2021), whether it be due to mass loss (Soker 2001; Adams et al. 2013) or planet–planet scattering (Kane & Raymond 2014; Carrera et al. 2019). Thus, the prospect of  $\iota$  Dra being a multi-planet system containing significantly eccentric orbits becomes a useful case study in the evolutionary history of planets orbiting evolved stars.

Precision RV surveys for exoplanets have now been operating for several decades, extending the period sensitivity toward Saturn analogs (Montet et al. 2014; Wittenmyer et al. 2020). However, the detection and characterization of planetary orbits outside the current observing window remains challenging due to the difficulties in reliably extracting Keplerian orbital parameters from data with partial phase coverage (Dalba et al. 2020a). A notable exception lies in the case of HR 5183b, whose eccentric  $\sim 74$  yr orbit was observed during periastron passage (Blunt et al. 2019), almost entering the Habitable Zone of the system (Kane & Blunt 2019). The orbital period of the



**Figure 11.** *orvara* posteriors for the mass of the star ( $M_{\text{pri}}$ ), mass of the outer companion ( $M_{\text{sec}}$ ), semimajor axis ( $a$ ), eccentricity ( $e$ ), and inclination ( $i$ ). Note the prior for  $M_{\text{pri}}$  was taken from our results in Table 2. By combining RV and proper-motion analysis, *orvara* provides a further constraint on the outer companion, with a posterior mass of  $17.0^{+13}_{-5.4} M_{\text{Jup}}$ , which puts the companion on the boundary between the planet and brown dwarf regimes. These results are tabulated in Table 4.

additional companion to  $\iota$  Dra described here, though relatively unconstrained, is similar in value to that of HR 5183b (see Table 4). Continued low-cadence monitoring of the system will constrain the eccentricity of the orbit, which, in turn, will provide further improvements to the orbital period without the need to observe a complete orbit.

Jitter estimates from well-sampled RV time series of giants are relatively rare. Studies of RV jitter made by Tayar et al. (2019) and Luhn et al. (2020) predict RV rms for stars similar to  $\iota$  Dra of  $12\text{--}16\text{ m s}^{-1}$  and  $15\text{ m s}^{-1}$ , respectively. The jitter terms in Table 3 are estimated to be slightly smaller than, but broadly consistent with, the predictions from these studies, with jitter  $\sigma_{\text{apf}} \sim 10\text{ m s}^{-1}$  and jitter  $\sigma_{\text{CAT}_{\text{HES}}} \sim 13.5\text{ m s}^{-1}$ . With a  $\log g$  of  $2.48 \pm 0.01$ ,  $\iota$  Dra is on the boundary of the stellar

samples included in these studies; future studies into the predictions of stellar jitter should be extended to include stars of lower  $\log g$ .

As noted by Kane et al. (2010), the large stellar radius of  $\iota$  Dra, combined with the favorable orientation of the highly eccentric planetary orbit, yields a transit probability of  $\sim 16\%$  for the known inner planet. TESS observations of  $\iota$  Dra during the initial mission cycles did not coincide with the expected time of inferior conjunction for  $\iota$  Dra b, and thus a transit of this planet has not yet been ruled out. However, subsequent TESS observations will revisit this star, providing further opportunities to detect a possible transit. The next window for this potential transit will occur at  $\text{BJD } 2459677.03 \pm 0.13$  (2022 April 7), when TESS will be in its 4+ year, and scheduled to

**Table 4**  
orvara Posteriors

Parameter	Planet b	Planet c	Units
<b>Fitted Parameters</b>			
Companion Mass ( $M_s$ )	$16.4^{+9.3}_{-4.0}$	$17.0^{+13}_{-5.4}$	$M_{\text{Jup}}$
Semimajor Axis ( $a$ )	$1.453^{+0.026}_{-0.026}$	$19.4^{+10}_{-7.7}$	au
$\sqrt{e} \sin \omega$	$0.8373^{+0.0010}_{-0.0010}$	$0.44^{+0.24}_{-0.64}$	
$\sqrt{e} \cos \omega$	$0.0015^{+0.0044}_{-0.0043}$	$0.46^{+0.15}_{-0.23}$	
Inclination	$46^{+27}_{-19}$	$86^{+19}_{-19}$	deg
Ascending node	$87^{+64}_{-60}$	$107^{+44}_{-59}$	deg
Mean longitude	$173.18^{+0.23}_{-0.24}$	$108.7^{+9.4}_{-13}$	deg
<b>Derived Parameters</b>			
Period	$1.398643^{+0.000035}_{-0.000035}$	$68^{+60}_{-36}$	yr
Argument of Periastron	$89.90^{+0.30}_{-0.30}$	$62^{+262}_{-32}$	deg
Eccentricity	$0.7010^{+0.0016}_{-0.0017}$	$0.455^{+0.12}_{-0.084}$	
Semimajor Axis	$47.26^{+0.83}_{-0.83}$	$630^{+328}_{-250}$	mas
$T_0$	$2455590.17^{+0.13}_{-0.13}$	$2476000^{+22000}_{-13000}$	JD
Mass ratio	$0.0100^{+0.0058}_{-0.0024}$	$0.0105^{+0.0080}_{-0.0034}$	
$M_p \sin i$	$11.82^{+0.42}_{-0.41}$	$15.6^{+14}_{-5.1}$	$M_{\text{Jup}}$
<b>Other Parameters</b>			
Jitter	$11.42^{+0.36}_{-0.33}$		$\text{m s}^{-1}$
Stellar Mass ( $M_{\text{pri}}$ )	$1.551^{+0.083}_{-0.078}$		$M_{\text{sun}}$
Parallax	$32.5224^{+0.0010}_{-0.0016}$		mas
Barycenter Proper-motion R.A.	$-8.23^{+0.60}_{-0.25}$		$\text{mas yr}^{-1}$
Barycenter Proper-motion decl.	$17.22^{+0.16}_{-0.33}$		$\text{mas yr}^{-1}$
RV Zero Point CAT_HES	$-14^{+29}_{-48}$		$\text{m s}^{-1}$
RV Zero Point APF	$-143^{+21}_{-49}$		$\text{m s}^{-1}$

observe Sector 50. Provided Sector 50 is observed on schedule,  $\iota$  Dra will be observed during this transit window and so any transit of  $\iota$  Dra b should be observed.

As a companion to a bright  $V = 3.3$  magnitude star, the brown dwarf orbiting  $\iota$  Dra could be a prime candidate for future direct imaging missions. At 30.74 pc away and with a semimajor axis of  $\sim 19.4$  au, the separation of  $\iota$  Dra and the outer companion is  $\sim 630$  mas. Assuming a radius of  $1 R_{\text{Jup}}$  and albedo of 0.5, the peak brightness of the companion is estimated to be  $\sim 2 \times 10^{-10}$ . With a predicted contrast ratio detection threshold of  $\sim 10^{-10}$ , the Habitable Exoplanet Observatory (HabEx) combined with star shade (Gaudi et al. 2020) will have the greatest ability to directly image the outer companion of  $\iota$  Dra, provided the noise estimation for the instrument is accurate. Other missions, such as the Nancy Grace Roman Space Telescope with no star shade and a limiting contrast ratio of  $\sim 1 \times 10^{-9}$  (Kasdin et al. 2020), are unlikely to be able to detect the companion.

## 6. Conclusions

Planets orbiting giant stars are fascinating systems that provide opportunities to examine the effects of stellar evolution on the dynamics of planetary orbits. The case of  $\iota$  Dra provides a relatively nearby multi-planet giant star system through which to study these effects through precise measurements of the stellar and planetary properties. Through our SED and asteroseismology analysis we refined the stellar parameters for  $\iota$  Dra. Using TESS observations of the star over 5 sectors, we were able to constrain the stellar radius to  $\sim 2\%$ , mass to  $\sim 6\%$ ,

and age to  $\sim 28\%$ . Investigation into the evolutionary state of the star points toward an RGB classification.

We obtained 456 new RV observations of  $\iota$  Dra with the Lick Observatory APF telescope between 2018 February and 2021 February. These RV observations, combined with those previously published, cover several orbital periods of the known planet, providing significant improvement to the orbital parameters. These in turn allowed us to detect curvature in the previously identified RV linear trend, which is likely caused by a previously undiscovered outer companion. After running a dynamical analysis with the MEGNO chaos indicator to determine the range of semimajor axis and eccentricity configurations that the orbiting body could exist within, we further constrained the possible orbits with The Joker. We then combined our RV data with astrometry from Gaia and Hipparcos with the help of orvara and were able to obtain a best-fit solution for the outer companion. This solution gave the outer companion a period of  $68^{+60}_{-36}$  years, and eccentricity of  $0.455^{+0.12}_{-0.084}$ .

The orvara preferred orbital solution for the substellar outer companion estimated a mass on the border of the planet and brown dwarf regimes. The exclusion of stellar mass companions from the speckle imaging presented in Kane et al. (2014) also suggests that the orbiting companion is substellar. As it is ambiguous as to whether the companion is burning deuterium, we are unable to confidently identify whether it is a planet or a brown dwarf. As brown dwarfs are relatively rare, with  $0.8^{+0.8}_{-0.5}\%$  of stars hosting a brown dwarf (Nielsen et al. 2019), this could be an important addition to the population of brown dwarfs. The relatively close proximity of  $\iota$  Dra to Earth will make this a prime target in future giant planet and brown dwarf characterization studies. Continued observations of this target will help refine the orbital parameters of the outer companion and confirm its classification as either a giant planet or a brown dwarf.

The results reported herein benefited from collaborations and/or information exchange within NASA’s Nexus for Exoplanet System Science (NExSS) research coordination network sponsored by NASA’s Science Mission Directorate. P.D. acknowledges support from a National Science Foundation Astronomy and Astrophysics Postdoctoral Fellowship under award AST-1903811. T.L.C. acknowledges support from the European Union’s Horizon 2020 research and innovation program under the Marie Skłodowska-Curie grant agreement No. 792848 (PULSATION). T.L.C. is supported by Fundação para a Ciência e a Tecnologia (FCT) in the form of a work contract (CEECIND/00476/2018). C.K. acknowledges support by Erciyes University Scientific Research Projects Coordination Unit under grant No. MAP-2020-9749. T.L. acknowledges the funding from the European Research Council (ERC) under the European Union’s Horizon 2020 research and innovation program (CartographyY GA. 804752). D.B. and M.S.C. acknowledge supported by FCT through the research grants UIDB/04434/2020, UIDP/04434/2020 and PTDC/FIS-AST/30389/2017, and by FEDER—Fundo Europeu de Desenvolvimento Regional through COMPETE2020—Programa Operacional Competitividade e Internacionalização (grant: POCI-01-0145-FEDER-030389). M.S.C. is supported by national funds through FCT in the form of a work contract. R.A.G. and S.N.B. acknowledge the support of the PLATO and GOLF CNES grants. S.M. acknowledges the support from the Spanish Ministry of Science and Innovation with the Ramon y Cajal fellowship number RYC-2015-17697 and with the grant No. PID2019-107187GB-I00. D.H. acknowledges support

from the Alfred P. Sloan Foundation, the National Aeronautics and Space Administration (80NSSC19K0379), and the National Science Foundation (AST-1717000). D.L.B. acknowledges support from the NASA TESS GI Program under awards 80NSSC18K1585 and 80NSSC19K0385. T.R.B. acknowledges support from the Australian Research Council (DP210103119).

*Software:* RadVel (Fulton et al. 2018, <https://github.com/California-Planet-Search/radvel>) lightkurve (Lightkurve Collaboration et al. 2018, <https://github.com/lightkurve/lightkurve>)<sup>26</sup>, DIAMONDS (Corsaro & De Ridder 2014, <https://github.com/EnricoCorsaro/DIAMONDS>) Background extension to DIAMONDS (Corsaro & De Ridder 2014, <https://github.com/EnricoCorsaro/Background>) FAMED (Corsaro et al. 2020, <https://github.com/EnricoCorsaro/FAMED>) REBOUND: MEGNO (Rein & Liu 2012, <https://github.com/hannorein/rebound>) The Joker (Price-Whelan et al. 2017, <https://github.com/adrn/thejoker>) htof [Brandt et al. submitted] (<https://github.com/gmbrandt/htof>), orvara (Brandt et al. 2021, <https://github.com/t-brandt/orvara>).

### Appendix A Individual Mode Frequencies

Table 5 lists all significant modes (i.e.,  $p_{\text{det}} \geq 0.993$ ) returned by FAMED. The term  $p_{\text{det}}$  is the peak detection probability based on a Bayesian model comparison as performed by FAMED. A peak is tested against the noise only if its height in the smoothed power spectrum is lower than 10 times the local level of the background, otherwise the peak is automatically considered as detected (denoted as “–”). A peak is deemed significant if  $p_{\text{det}} \geq 0.993$ . See Section 5.3 of Corsaro et al. (2020) for details. The List column indicates which list each mode belongs to: Min. = Belongs to Minimal List; Max. = Belongs to Maximal List (but not to Minimal List).

**Table 5**  
Observed Mode Frequencies

$\ell$	Frequency ( $\mu\text{Hz}$ )	$1\sigma$ Uncertainty ( $\mu\text{Hz}$ )	$p_{\text{det}}$ <sup>a</sup>	List <sup>b</sup>
1	30.384	0.028	0.997	Min.
2	31.538	0.133	1.000	Min.
0	32.024	0.024	0.998	Min.
1	33.913	0.088	1.000	Min.
2	35.410	0.039	...	Min.
0	35.878	0.035	...	Min.
1	37.983	0.035	...	Min.
2	39.361	0.072	...	Min.
0	39.904	0.049	...	Min.
3	40.684	0.056	1.000	Max.
1	42.078	0.024	...	Max.
1	42.552	0.016	...	Min.
1	43.063	0.011	...	Max.
2	43.530	0.107	...	Min.
0	43.925	0.016	...	Max.
1	45.980	0.027	...	Min.
2	47.364	0.072	...	Min.
0	48.015	0.038	...	Min.
1	49.948	0.027	...	Min.
1	50.420	0.022	0.997	Max.
1	54.274	0.021	0.999	Min.
2	55.202	0.100	0.999	Max.
0	55.565	0.025	0.994	Max.

#### Notes.

<sup>a</sup> Peak detection probability based on a Bayesian model comparison as performed by FAMED. A peak is tested against the noise only if its height in the smoothed power spectrum is lower than 10 times the local level of the background, otherwise the peak is automatically considered as detected (denoted as “–”). A peak is deemed significant if  $p_{\text{det}} \geq 0.993$ . See Section 5.3 of Corsaro et al. (2020) for details.

<sup>b</sup> Min. = Belongs to Minimal List; Max. = Belongs to Maximal List (but not to Minimal List).


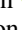







<sup>26</sup> See also the implementation of lightkurve: [https://github.com/hvipy/tessbkgd/blob/stable/notebooks/iot\\_Dra\\_tpf.ipynb](https://github.com/hvipy/tessbkgd/blob/stable/notebooks/iot_Dra_tpf.ipynb).

## Appendix B

### Stellar Model Grid Description

We used Modules for Experiments in Stellar Astrophysics (MESA, version 12115) to construct a grid of stellar models. General descriptions of the input physics and numerical methods can be found in the MESA papers (Paxton et al. 2011, 2013, 2015, 2018). We adopted the solar chemical mixture  $[(Z/X)_{\odot} = 0.0181]$  provided by Asplund et al. (2009). We used the MESA  $\rho$ - $T$  tables based on the 2005 update of the OPAL equation of state tables (Rogers & Nayfonov 2002) and we used OPAL opacities supplemented by the low-temperature opacities from Ferguson et al. (2005). The MESA “simple” photosphere was used for the set of boundary conditions for modeling the atmosphere; alternative model atmosphere choices do not strongly affect the results for solar-like oscillators (Yildiz 2007; Joyce & Chaboyer 2018; Nsamba et al. 2018; Viani et al. 2018) or for  $\delta$  Sct stars (Murphy et al., in review). The mixing-length theory of convection was implemented, where  $\alpha_{\text{MLT}} = \ell_{\text{MLT}}/H_p$  is the mixing-length parameter. The exponential scheme by Herwig (2000) was adopted for the convective overshooting. We defined the overshooting parameter as  $f_{\text{ov}} = (0.13 M_* - 0.098)/9.0$  and adopted a fixed  $f_{\text{ov}}$  of 0.018 for models with a mass above  $2.0 M_{\odot}$ , following the mass-overshooting relation found by Magic et al. (2010). We also applied the MESA predictive mixing scheme in our model for a smooth convective boundary. The mass-loss rate on the red-giant branch follows the Reimers’ prescription with  $\eta = 0.2$ , which is constrained by the old open clusters NGC 6791 and NGC 6819 (Miglio et al. 2012). Models in the grid varied in stellar mass within  $0.8$ – $2.2 M_{\odot}$  in steps of  $0.02 M_{\odot}$ , in initial helium fraction ( $Y_{\text{init}}$ ) within  $0.24$ – $0.32$  in steps of  $0.02$ , and in initial metallicity ( $[\text{Fe}/\text{H}]$ ) within  $-0.5$ – $0.5$  in steps of  $0.1$ . Moreover, four values were considered for the mixing-length parameter associated with the description of convection, namely,  $\alpha_{\text{MLT}} = 1.7, 1.9, 2.1$ , and  $2.3$ .

### ORCID iDs

Michelle L. Hill  <https://orcid.org/0000-0002-0139-4756>  
 Stephen R. Kane  <https://orcid.org/0000-0002-7084-0529>  
 Tiago L. Campante  <https://orcid.org/0000-0002-4588-5389>  
 Zhexiong Li  <https://orcid.org/0000-0002-4860-7667>  
 Paul A. Dalba  <https://orcid.org/0000-0002-4297-5506>  
 Timothy D. Brandt  <https://orcid.org/0000-0003-2630-8073>  
 Timothy R. White  <https://orcid.org/0000-0002-6980-3392>  
 Benjamin J. S. Pope  <https://orcid.org/0000-0003-2595-9114>  
 Keivan G. Stassun  <https://orcid.org/0000-0002-3481-9052>  
 Benjamin J. Fulton  <https://orcid.org/0000-0003-3504-5316>  
 Enrico Corsaro  <https://orcid.org/0000-0001-8835-2075>  
 Tanda Li  <https://orcid.org/0000-0001-6396-2563>  
 J. M. Joel Ong  <https://orcid.org/0000-0001-7664-648X>  
 Timothy R. Bedding  <https://orcid.org/0000-0001-5222-4661>  
 Diego Bossini  <https://orcid.org/0000-0002-9480-8400>  
 Derek L. Buzasi  <https://orcid.org/0000-0002-1988-143X>  
 William J. Chaplin  <https://orcid.org/0000-0002-5714-8618>  
 Margarida S. Cunha  <https://orcid.org/0000-0001-8237-7343>  
 Rafael A. García  <https://orcid.org/0000-0002-8854-3776>  
 Sylvain N. Breton  <https://orcid.org/0000-0003-0377-0740>  
 Marc Hon  <https://orcid.org/0000-0003-2400-6960>  
 Daniel Huber  <https://orcid.org/0000-0001-8832-4488>  
 Chen Jiang  <https://orcid.org/0000-0002-7614-1665>

Cenk Kayhan  <https://orcid.org/0000-0001-9198-2289>  
 James S. Kuszlewicz  <https://orcid.org/0000-0002-3322-5279>  
 Savita Mathur  <https://orcid.org/0000-0002-0129-0316>  
 Aldo Serenelli  <https://orcid.org/0000-0001-6359-2769>  
 Dennis Stello  <https://orcid.org/0000-0002-4879-3519>

### References

- Adams, F. C., Anderson, K. R., & Bloch, A. M. 2013, *MNRAS*, **432**, 438  
 Asplund, M., Grevesse, N., Sauval, A. J., & Scott, P. 2009, *ARA&A*, **47**, 481  
 Assef, R. J., Gaudi, B. S., & Stanek, K. Z. 2009, *ApJ*, **701**, 1616  
 Baines, E. K., McAlister, H. A., ten Brummelaar, T. A., et al. 2011, *ApJ*, **743**, 130  
 Barnes, J. W. 2007, *PASP*, **119**, 986  
 Bedding, T. R., Kjeldsen, H., Campante, T. L., et al. 2010, *ApJ*, **713**, 935  
 Bedding, T. R., Mosser, B., Huber, D., et al. 2011, *Natur*, **471**, 608  
 Bergmann, C., Jones, M. I., Zhao, J., et al. 2021, *PASA*, **38**, e019  
 Blunt, S., Endl, M., Weiss, L. M., et al. 2019, *AJ*, **158**, 181  
 Brandt, T. D. 2018, *ApJS*, **239**, 31  
 Brandt, T. D. 2021, *ApJS*, **254**, 42  
 Brandt, T. D., Dupuy, T. J., Li, Y., et al. 2021, arXiv:2105.11671  
 Butler, R. P., Wright, J. T., Marcy, G. W., et al. 2006, *ApJ*, **646**, 505  
 Campante, T. L., Corsaro, E., Lund, M. N., et al. 2019, *ApJ*, **885**, 31  
 Campante, T. L., Handberg, R., Mathur, S., et al. 2011, *A&A*, **534**, A6  
 Campante, T. L., Schofield, M., Kuszlewicz, J. S., et al. 2016, *ApJ*, **830**, 138  
 Campante, T. L., Veras, D., North, T. S. H., et al. 2017, *MNRAS*, **469**, 1360  
 Carrera, D., Raymond, S. N., & Davies, M. B. 2019, *A&A*, **629**, L7  
 Christensen-Dalsgaard, J., Silva Aguirre, V., Elsworth, Y., & Hekker, S. 2014, *MNRAS*, **445**, 3685  
 Cincotta, P. M., & Simó, C. 2000, *A&AS*, **147**, 205  
 Corsaro, E., & De Ridder, J. 2014, *A&A*, **571**, A71  
 Corsaro, E., McKeever, J. M., & Kuszlewicz, J. S. 2020, *A&A*, **640**, A130  
 Dalba, P. A., Fulton, B., Isaacson, H., Kane, S. R., & Howard, A. W. 2020a, *AJ*, **160**, 149  
 Dalba, P. A., Gupta, A. F., Rodriguez, J. E., et al. 2020b, *AJ*, **159**, 241  
 Dalba, P. A., Kane, S. R., Barclay, T., et al. 2019, *PASP*, **131**, 034401  
 Damiani, C., & Mathis, S. 2018, *A&A*, **618**, A90  
 Duncan, M. J., Levison, H. F., & Lee, M. H. 1998, *AJ*, **116**, 2067  
 Eisner, N. L., Pope, B. J. S., Aigrain, S., et al. 2019, *RNAAS*, **3**, 145  
 ESA 1997, The Hipparcos and Tycho Catalogues, ESA SP-1200 (Noordwijk: ESA)  
 Farr, W. M., Pope, B. J. S., Davies, G. R., et al. 2018, *ApJL*, **865**, L20  
 Ferguson, J. W., Alexander, D. R., Allard, F., et al. 2005, *ApJ*, **623**, 585  
 Ford, E. B. 2014, *PNAS*, **111**, 12616  
 Foreman-Mackey, D., Hogg, D. W., Lang, D., & Goodman, J. 2013, *PASP*, **125**, 306  
 Frink, S., Mitchell, D. S., Quirrenbach, A., et al. 2002, *ApJ*, **576**, 478  
 Fulton, B. J., Petigura, E. A., Blunt, S., & Sinukoff, E. 2018, *PASP*, **130**, 044504  
 Gaia Collaboration, Brown, A. G. A., Vallenari, A., et al. 2018, *A&A*, **616**, A1  
 Gaia Collaboration, Brown, A. G. A., Vallenari, A., et al. 2021, *A&A*, **650**, C3  
 Gaia Collaboration, Prusti, T., de Bruijne, J. H. J., et al. 2016, *A&A*, **595**, A1  
 Gallet, F., Charbonnel, C., Amard, L., et al. 2017, *A&A*, **597**, A14  
 García Saravia Ortiz de Montellano, A., Hekker, S., & Themeßl, N. 2018, *MNRAS*, **476**, 1470  
 Gaudi, B. S., Seager, S., Mennesson, B., et al. 2020, arXiv:2001.06683  
 Gould, B. A. 1855, *AJ*, **4**, 81  
 Grunblatt, S. K., Huber, D., Gaidos, E., et al. 2018, *ApJ*, **861**, L5  
 Grunblatt, S. K., Huber, D., Gaidos, E., et al. 2019, *AJ*, **158**, 227  
 Handberg, R., & Campante, T. L. 2011, *A&A*, **527**, A56  
 Hastings, W. K. 1970, *Biometrika*, **57**, 97  
 Hatzes, A. P., Endl, M., Cochran, W. D., et al. 2018, *AJ*, **155**, 120  
 Hekker, S., & Meléndez, J. 2007, *A&A*, **475**, 1003  
 Herwig, F. 2000, *A&A*, **360**, 952  
 Hinde, T. C., Christou, A. A., Alvarellos, J. L. A., & Goździewski, K. 2010, *MNRAS*, **404**, 837  
 Hon, M., Stello, D., & Yu, J. 2017, *MNRAS*, **469**, 4578  
 Hon, M., Stello, D., & Yu, J. 2018, *MNRAS*, **476**, 3233  
 Horch, E. P., Veilleux, D. R., Baena Gallé, R., et al. 2009, *AJ*, **137**, 5057  
 Howard, A. W., Johnson, J. A., Marcy, G. W., et al. 2010, *ApJ*, **721**, 1467  
 Huber, D., Stello, D., Bedding, T. R., et al. 2009, *CoAst*, **160**, 74  
 Jofré, E., Petrucci, R., Saffe, C., et al. 2015, *A&A*, **574**, A50  
 Jones, M. I., Jenkins, J. S., Bluhm, P., Rojo, P., & Melo, C. H. F. 2014, *A&A*, **566**, A113

- Joyce, M., & Chaboyer, B. 2018, *ApJ*, **856**, 10
- Kallinger, T., Hekker, S., Mosser, B., et al. 2012, *A&A*, **541**, A51
- Kane, S. R., & Blunt, S. 2019, *AJ*, **158**, 209
- Kane, S. R., Howell, S. B., Horch, E. P., et al. 2014, *ApJ*, **785**, 93
- Kane, S. R., & Raymond, S. N. 2014, *ApJ*, **784**, 104
- Kane, S. R., Reffert, S., Henry, G. W., et al. 2010, *ApJ*, **720**, 1644
- Kane, S. R., & von Braun, K. 2008, *ApJ*, **689**, 492
- Kasdin, N. J., Bailey, V. P., Mennesson, B., et al. 2020, *Proc. SPIE*, **11443**, 114431U
- Keenan, P. C., & McNeil, R. C. 1989, *ApJS*, **71**, 245
- Kipping, D. M. 2013, *MNRAS*, **434**, L51
- Kuslewicz, J. S., Hekker, S., & Bell, K. J. 2020, *MNRAS*, **497**, 4843
- Lenz, P., & Breger, M. 2005, *CoAst*, **146**, 53
- Li, T., Bedding, T. R., Christensen-Dalsgaard, J., et al. 2020, *MNRAS*, **495**, 3431
- Lightkurve Collaboration, Cardoso, J. V. D. M. A., Hedges, C., et al. 2018, *Lightkurve: Kepler and TESS time series analysis in Python*, Astrophysics Source Code Library, ascl:[1812.013](#)
- Luhn, J. K., Wright, J. T., Howard, A. W., & Isaacson, H. 2020, *AJ*, **159**, 235
- Magic, Z., Serenelli, A., Weiss, A., & Chaboyer, B. 2010, *ApJ*, **718**, 1378
- Mathur, S., García, R. A., Régulo, C., et al. 2010, *A&A*, **511**, A46
- Mermilliod, J. C. 2006, *yCat*, **II/168**
- Metropolis, N., Rosenbluth, A. W., Rosenbluth, M. N., Teller, A. H., & Teller, E. 1953, *JChPh*, **21**, 1087
- Miglio, A., Brogaard, K., Stello, D., et al. 2012, *MNRAS*, **419**, 2077
- Montet, B. T., Crepp, J. R., Johnson, J. A., Howard, A. W., & Marcy, G. W. 2014, *ApJ*, **781**, 28
- Mosser, B., & Appourchaux, T. 2009, *A&A*, **508**, 877
- Mosser, B., Barban, C., Montalbán, J., et al. 2011, *A&A*, **532**, A86
- Nielsen, E. L., De Rosa, R. J., Macintosh, B., et al. 2019, *AJ*, **158**, 13
- Nsamba, B., Campante, T. L., Monteiro, M. J. P. F. G., et al. 2018, *MNRAS*, **477**, 5052
- Paunzen, E. 2015, *A&A*, **580**, A23
- Paxton, B., Bildsten, L., Dotter, A., et al. 2011, *ApJS*, **192**, 3
- Paxton, B., Cantiello, M., Arras, P., et al. 2013, *ApJS*, **208**, 4
- Paxton, B., Marchant, P., Schwab, J., et al. 2015, *ApJS*, **220**, 15
- Paxton, B., Schwab, J., Bauer, E. B., et al. 2018, *ApJS*, **234**, 34
- Peirce, B. 1852, *AJ*, **2**, 161
- Price-Whelan, A. M., Hogg, D. W., Foreman-Mackey, D., & Rix, H.-W. 2017, *ApJ*, **837**, 20
- Radovan, M. V., Lanclos, K., Holden, B. P., et al. 2014, *Proc. SPIE*, **9145**, 91452B
- Reffert, S., Bergmann, C., Quirrenbach, A., Trifonov, T., & Künstler, A. 2015, *A&A*, **574**, A116
- Rein, H., & Liu, S. F. 2012, *A&A*, **537**, A128
- Rein, H., & Tamayo, D. 2015, *MNRAS*, **452**, 376
- Ricker, G. R., Winn, J. N., Vanderspek, R., et al. 2015, *JATIS*, **1**, 014003
- Rogers, F. J., & Nayfonov, A. 2002, *ApJ*, **576**, 1064
- Soker, N. 2001, *MNRAS*, **324**, 699
- Stassun, K. G., Collins, K. A., & Gaudi, B. S. 2017, *AJ*, **153**, 136
- Stassun, K. G., Corsaro, E., Pepper, J. A., & Gaudi, B. S. 2018a, *AJ*, **155**, 22
- Stassun, K. G., & Torres, G. 2016, *AJ*, **152**, 180
- Stassun, K. G., & Torres, G. 2018, *ApJ*, **862**, 61
- Stassun, K. G., Oelkers, R. J., Pepper, J., et al. 2018b, *AJ*, **156**, 102
- Tayar, J., Stassun, K. G., & Corsaro, E. 2019, *ApJ*, **883**, 195
- Torres, G., Andersen, J., & Giménez, A. 2010, *A&ARv*, **18**, 67
- Torres, G., Fischer, D. A., Sozzetti, A., et al. 2012, *ApJ*, **757**, 161
- van Leeuwen, F. 2007, *A&A*, **474**, 653
- Viani, L. S., Basu, S., Corsaro, E., Ball, W. H., & Chaplin, W. J. 2019, *ApJ*, **879**, 33
- Viani, L. S., Basu, S., Ong, J. M. J., Bonaca, A., & Chaplin, W. J. 2018, *ApJ*, **858**, 28
- Vogt, S. S., Radovan, M., Kibrick, R., et al. 2014, *PASP*, **126**, 359
- Vrard, M., Mosser, B., & Samadi, R. 2016, *A&A*, **588**, A87
- Winn, J. N., & Fabrycky, D. C. 2015, *ARA&A*, **53**, 409
- Wittenmyer, R. A., Jones, M. I., Zhao, J., et al. 2017, *AJ*, **153**, 51
- Wittenmyer, R. A., Wang, S., Horner, J., et al. 2020, *MNRAS*, **492**, 377
- Yildiz, M. 2007, *MNRAS*, **374**, 1264
- Zechmeister, M., Reffert, S., Hatzes, A. P., Endl, M., & Quirrenbach, A. 2008, *A&A*, **491**, 531